Thermal-mechanical analysis on the mass loss of high-speed projectiles penetrating concrete targets

Lei Guo [a, b], Yong He [a, *], Xianfeng Zhang [a], Yuan He [a], Jiajie Deng [a], Zhongwei Guan [b]

[a] *School of Mechanical Engineering, Nanjing University of Science & Technology, Nanjing 210094, PR China*
[b] *School of Engineering, University of Liverpool, Brownlow Street, Liverpool L69 3GQ, United Kingdom*

A R T I C L E   I N F O

A B S T R A C T

The significant mass loss of the kinetic energy (KE) projectile has been observed in the high-speed penetration (usually $v_0 > 1$ km/s) into concrete target, resulting in nose abrasion, bending, and trajectory deviation as well as great drop of the Depth of Penetration (DOP). The thermoplastic failure of material peeling from the thin exterior interface between the projectile and the concrete is the main mechanism of the mass loss. Combining the heat generated from the friction work and the plastic deformation work during the high-speed penetration process, a discrete iterative method is proposed to investigate the movement and the nose shape variation on the basis of thermoplastic instability of the material. Utilizing the temperature-based failure criterion and the Johnson-Cook (J-C) constitutive model, the receding displacements of the discrete points are determined by the gradient distribution of the temperature change along the depth from the surface of a projectile, which result in blunting of the projectile nose. The predictions of the nose shape, the percentage of the mass loss and the DOP were validated against the experimental data. Then further studies are conducted to investigate the critical velocity of mass loss and the "secondary peak" deceleration. The onset of the mass loss and the occurrence of the distinct pulse of the deceleration in the tunnel stage are regarded as the symbol of the lower and upper velocity limits of the nondeformable penetration regime. In addition, through the comparison of the percentages of heat generated with different mechanisms at different locations of the projectile, the dominant mechanism of the mass loss between the friction and plastic deformation is analyzed to get an insight into the high-speed penetration process.

1. Introduction

Deep penetration of the high-speed kinetic energy (KE) projectile into concrete target has intrigued the weapon designers due to the rapid development of constructions of both ground and underground military fortifications protected by reinforced concrete. The theoretical models published previously (Rosenberg and Dekel, 2009; Tate, 1967; Kennedy, 1976; Li and Chen, 2003) were mainly based on the hypothesis of "rigid" projectile in the low-speed penetration range ($v_0 < 1$ km/s), ignoring the influence of mass abrasion occurred at the projectile. However, with increasing the impact velocity (1 km/s $< v_0 <$ 2 km/s), the earth penetration weapon (EPW) may face the problem of structural integrity caused by the serious mass loss. The related phenomena, such as nose abrasion, bending or breaking of the projectile, were observed in many penetration experiments (Alekseevskii, 1966; Forrestal et al., 1996; LundgrenHigh-velocit, 1994; Frew et al., 1998), resulting in the trajectory deviation as well as dramatic drop of Depth of Penetration (DOP). Studying mechanisms of the mass loss of a projectile during high-speed penetration has been a topic of interest in the international research community, especially in the weapon development and engineering protection field.

The systematic experimental research on penetration experiments into concrete and grout targets was conducted by Forrestal et al. (1996) and Frew et al. (1998,2000,2006), which produce the most authoritative experimental data. Mass loss up to 7% of the original projectile was recorded when the striking velocity exceeds 1200 m/s, resulting in a dramatic decline of the DOP. Similar experimental investigation was undertaken by He et al. (2010a) and Yang et al. (2012a), which mainly focused on the transition from

Nomenclature

Parameter	Units	Parameter in Johnson-Cook model
A	MPa	Instant deceleration of projectile
a	m/s^2	Parameter in Johnson-Cook model
B	MPa	Instant length of projectile nose
b	m	Initial length of projectile nose
b_0	m	Parameter in Johnson-Cook model
C		Heat capacity of projectile
c_p	J/(kg·K)	Heat capacity of concrete
c_c	J/(kg·K)	Diameter of projectile
d	m	Resistance force on the nose of projectile along the X axis
F_x	N	Unconfined compressive strength of concrete
f_c	MPa	Frictional force on projectile
f	MPa	Shear modulus
G	GPa	Thermal conductivity of projectile
k_p	W/(m·K)	Thermal conductivity of concrete
k_c	W/(m·K)	Dimensionless factor for the depth of crater stage
k'		Constant parameter in Eq. (11)
k_1	MPa·s/m	Constant parameter in Eq. (11)
k_2		Length of projectile
L_p	m	Width of the each discrete stick
l_c	m	Instant mass of projectile
M	kg	Initial mass of projectile
M_0	kg	Parameter in Johnson-Cook model
m		Parameter in Johnson-Cook model
n		Discrete number of the HAZ
n_{xHAZ}		Discrete number of each time step Δt.
n_{tHAZ}		Total discrete number of penetration time
ni		Total discrete number along the radius
nj		Nose factor in Eq. (1)
N		Normal pressure on projectile
p	MPa	Constant parameter in Eq. (13)
p^*		Heat generation by friction
Q	J	Heat generation by friction conducted into projectile
Q_p	J	Heat generation by friction conducted into concrete
Q_c	J	Dynamic strength parameter of concrete

(*continued*)

Parameter	Units	Description
R_c	MPa	Radius of projectile
r	m	Dimensionless constant
S		Initial temperature
T_0	K	Critical temperature
T_{cr}	K	Parameter in Eq. (18)
T_{DRX}	K	Melting temperature
T_m	K	Temperature distribution generated by friction
T_t	K	Temperature distribution generated by plastic work converted to heat
T_a	K	Total temperature distribution
T_{total}	K	Instant velocity of projectile
v	m/s	Critical velocity for mass loss
v_s	m/s	Initial velocity of projectile
v_0	m/s	Instant tangential velocity of projectile in Fig. 2
v_τ	m/s	Instant normal velocity of projectile in Fig. 2
v_n	m/s	The width of the HAZ
w_{HAZ}	μm	The width of the ASB
w_{ASB}	μm	Depth of the crater stage
Z_1	m	Instant depth of penetration
z	m	Constant parameter in Eq. (11)
α		Plastic work to heat conversion factor.
β		The percentage of mass loss
γ		The angle in Fig. 2
φ		$\theta=\pi/2-\varphi$
θ		CRH (caliber-radius-head) for ogival nose
Ψ		The effective strain rate at the contact shear plane AB
$\dot{\varepsilon}_{AB}$	s^{-1}	The effective strain at the contact shear plane AB
$\overline{\varepsilon}_{AB}$		Parameter in Eq. (18)
$\dot{\varepsilon}_{DRX}$	s^{-1}	Coefficient of friction
μ		Density of projectile material
ρ_p	kg/m^3	Density of concrete
ρ_c	kg/m^3	
Superscript		Number of time steps
i		
Subscript		Sequence number in spatial dimension
j		Parameter in Johnson-Cook model

rigid to deformable penetration state with various strengths of the projectiles. It was shown that the curved trajectory, erosion and bending of projectiles are the common phenomena in the high-speed penetration. Furthermore, Silling et al (Silling and Forreatal, 2007). established a linearly proportional relationship, through empirical fitting of the experimental data, between the mass abrasion and the initial kinetic energy of a projectile below the velocity of 1000 m/s. Meanwhile, Chen et al. (2010) summarized the experimental data (Forrestal et al., 1996; Frew et al., 1998) and pointed out that the mass loss is closely related to the striking velocity of the penetrator and the category of the aggregate casted in the concrete target. Obviously, figuring out the influence of heat generated by dynamic friction between the projectile and targets is essential for understanding the thermo-mechanical mass loss process of a projectile. Klepaczko and Hughes (2005) conducted a theoretical investigation into the surface layer thermodynamics of steel projectile and proposed universal parameters, such as the rate of wear and rate sensitivity of wear. Recently, Guo et al. (2014) undertook a systematic investigation on the surface evolution of the recovered projectile subjected to a high-speed penetration at the microscopic scale. Microstructural features, including the mixed zone (MZ), the refined zone (RZ) and original zone (OZ), were analyzed respectively. In addition, the underlying mechanisms of the mass loss during high-speed penetration were demonstrated.

Due to the complex transient characteristics of the high-speed penetration process, it is very difficult to record the real-time physical parameters in experiments. Relevant theoretical research is necessary to reveal the underlying mechanisms of the mass loss. Based on the assumption that the heat converted from friction work melt the material on the nose of the projectile, an approximate analytical solution was presented by Jones et al. (2002a, 2003). to estimate a quantitative value of mass loss. The calculated results showed that the mass loss was directly proportional to the tunnel length, the diameter of projectile and the shear strength of target. Later, Beissel and Johnson (2000,2002). presented a surface abrasion criterion that is proportional to the relative sliding velocity and the normal stress between projectile and target. This criterion was incorporated in an axisymmetric finite-element algorithm with a fully rezoning method. It was found that numerical predictions were in a reasonable agreement with the available literature experimental data. Considering the velocity-dependent friction, an analytical incremental model was applied by Davis et al. (2003) to investigate the mass loss and to assess the projectile's performance in terms of its wear characteristics. Chen et al. (2010) also proposed an engineering abrasion model, based on the graphical discussion on the nose of the residual projectiles after high-speed penetration into concrete. Besides, utilizing Chen's model (Chen et al., 2010), further analyses were carried out by He and Chen (2011a), He et al. (2014) to discuss about the characteristic parameters of the projectile during penetration. It was demonstrated that the pulse shape of deceleration during high-speed penetration with mass loss was quite different from the "rigid" case. Moreover, taking into account scratch and heat melt effects pointed out by Jones et al. (2002a) and Davis et al. (2003) respectively, He et al. (2010b) suggested an empirical expression to estimate the mass loss rate with seven main influential variables, i.e. the initial nose shape, initial impact velocity, melting heat, shank diameter of a projectile, density and strength of the target as well as aggregate hardness of the target. The effects of these variables on the ultimate mass loss of a penetrator were compared, which provided useful information for engineering

applications. Moreover, in order to predict the DOP of a projectile with mass loss, several analytical formula were developed empirically or semi-empirically by fitting the experimental data to calculate the upper limit DOP of the high-speed projectile (Wen et al., 2010; Yang et al., 2012b; Mu and Zhang, 2011; Zhao et al., 2010a, 2012; Wu et al., 2012; He and Chen, 2011b). In general, the existing abrasion models are mainly based on the assumption that the mass loss is totally resulted from the peeling of the molten surface material or derived by fitting the experimental results. Hence, an appropriate mass loss model involving the mechanisms of mass loss is necessary to study the high-speed penetration process into concrete.

In consideration of the thermoplastic material failure of the projectile, the present study attempts to develop a theoretical mass loss model to investigate the thermo-mechanical penetration process. The temperature rise located in the thin exterior interface of the projectile is derived from the heat conduction by the high-speed sliding friction and the plastic work converted to heat. Utilizing the iterative incremental calculations, the receding displacement of the discrete point is determined for each time step according to the temperature-based failure criteria of the plasticity instability. The predictions of the nose shape variation, the percentage of the mass loss and the DOP are validated with the experimental data. Furthermore, compared with rigid penetration, the detailed parametric studies are conducted to reveal the characteristic features of the penetration process and the dominant factors that influence the mass loss.

2. Thermoplastic mass abrasion model for projectile

2.1. Penetration process including mass loss

Coupling with the extremely high pressure and temperature, serious mass abrasion occurs in the thin exterior interface of a projectile during the high velocity penetration, resulting in structural failure and ballistic trajectory deflection. Moreover, asymmetrical stress on the surface of the projectile will be aggravated due to the inhomogeneous distribution of aggregate in concrete, determining the complexity of the high-speed penetration process. The published experimental observations (Forrestal et al., 1996; Frew et al., 1998; He et al., 2010a) have shown that the mass loss mostly takes place on the nose of the projectile, while the diameter of the shank ($d = 2r$) remains approximately constant during penetration. Thus the variations of the projectile's nose shape are the research emphasis for understanding of the high-speed penetration with mass loss.

Assuming that the penetration trajectory keeps straight without deflection, the high-speed penetration into a semi-infinite concrete target can be generally divided into two stages from various post-test observations (Forrestal et al., 2003; Luk and Forrestal, 1987), i.e. crater stage ($z \leq Z_1$) and tunnel stage ($z \geq Z_1$). As shown in Fig. 1, a global coordinate system R-Z is established to investigate the high-speed penetration into a semi-infinite concrete target. Compared with the tunnel stage, the mass loss and deformation occurred on the crater stage can be negligible due to its relatively short duration of time and displacement. Theoretical formulas were proposed by Forrestal et al. (1994). to predict the residual velocity v_1 and the instant depth Z_1 at the end of the crater stage, given by:

$$v_1{}^2 = \frac{M_0 v_0{}^2 - (\pi k' d^3/4)R_c}{M_0 + (\pi k' d^3/4)N\rho_c} \quad (1)$$

$$Z_1 = 2k'r \quad (2)$$

where M_0 and v_0 are the initial mass and velocity of a projectile, respectively. The parameter r is the radius of the projectile. ρ_c is the density of concrete. R_c is the target resistance parameter, $R_c = Sf_c$ (Forrestal et al., 1994, 1996) is applicable under certain condition for the small size penetration event, where f_c is the unconfined compressive strength of the concrete. And $S = 82.6f_c^{-0.544}$ is an empirical constant (Li and Chen, 2003; Frew et al., 1998) derived by curve fitting to available data. This expression is applicable for the specific experimental projectile-target configurations used in this study. However, this empirical relation does not hold in general for all either large or small projectile-target configurations (Forrestal et al., 2003). N is a nose factor and has the expression (Li and Chen, 2003; Forrestal et al., 1994) as $N=(8\Psi-1)/24\Psi^2$, where Ψ is the initial CRH (caliber-radius-head) of the ogive nose. The parameter k' is a dimensionless factor for high velocity penetration events with striking velocities greater than 1 km/s. The empirical $k'=(0.707 + b_0/2r)$ is derived from the experimental data in references (Li and Chen, 2003; He and Chen, 2011a). b_0 is the initial length of the projectile nose.

The penetration theory of the dynamic spherical cavity expansion for concrete was originally developed by Forrestal and Tzou (1997). It is based on the idealized Mohr-Coulomb with a tension cutoff and can be used to estimate the pressure imposed on the nose of a projectile during penetration. The Mohr-Coulomb and Drucker-Prager yield criteria are the same under certain condition for the spherical cavity-expansion problem. The curve-fitting normal pressure p is expressed as:

$$p = Sf_c + \rho_c v_n{}^2 \quad (3)$$

where $v_n = v\cos\varphi$ is the cavity-expansion velocity at the nose-target interface caused by projectile penetration, and φ is the angle between the axis of the penetrator and the normal direction of the nose surface, as shown in Fig. 2. The value of φ at the nose tip can be expressed as $\varphi_0 = \sin^{-1} [(2\psi\text{-}1)/\psi]$ (Forrestal and Luk, 1992). The friction is proportional to the normal pressure p. Taking the friction coefficient as μ, the friction can be expressed as:

$$f = \mu p \quad (4)$$

Understanding the localized interaction between the surfaces of a projectile and a concrete target is essential to study the mass loss of the projectile. Guo et al. (2014) and Lu (2002) have systematically studied the microstructural transformation mechanisms of a projectile subjected to high-speed penetration, which include the thermal softening, material flow and eventual mass loss associated with high strains and high-strain rates at high temperature. As a significant influence factor in the mass loss of the penetrator, the effect of temperature rise on the thermodynamic behavior of projectile material becomes remarkable with continual enhancement of striking velocity.

In order to predict the material peeled from the surface layer of a projectile, temperature rising concentrated in the thin exterior interface of the projectile during penetration process needs to be calculated quantitatively. According to the mass loss mechanisms mentioned above, two main modes of heat generation in the projectile and the concrete must be considered: the projectile/concrete surface friction heat and the heat converted from the plastic deformation of the projectile. High-speed surface friction between the projectile and the concrete can generate a tremendous amount of heat, transmitting from the exterior surface to the interior of the projectile. The distance of heat conduction, depended on the penetration time or the impact velocity as well as the heat
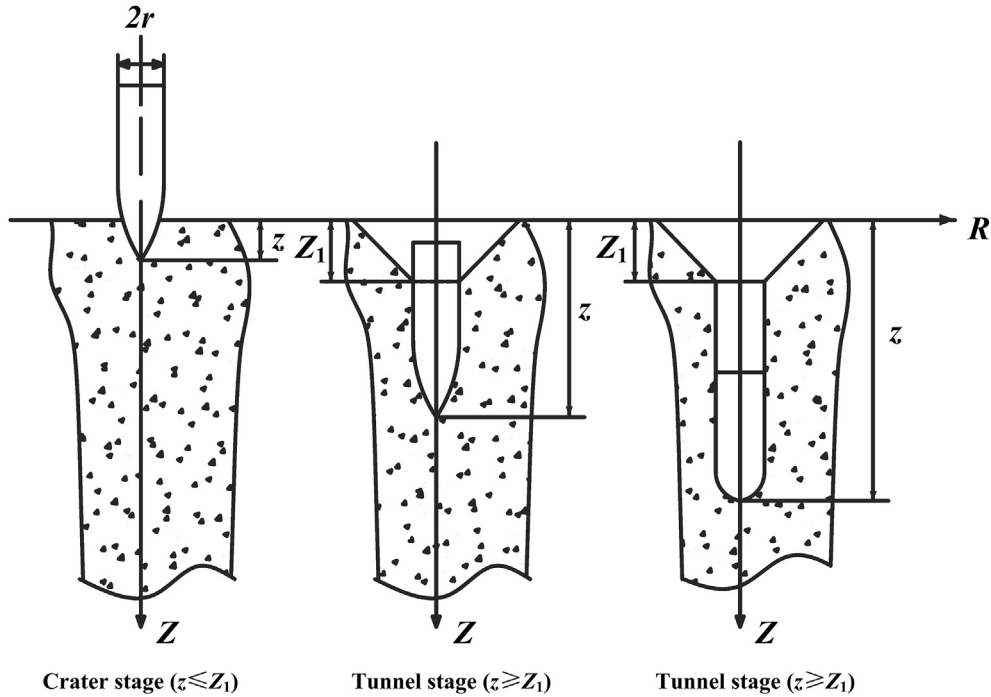
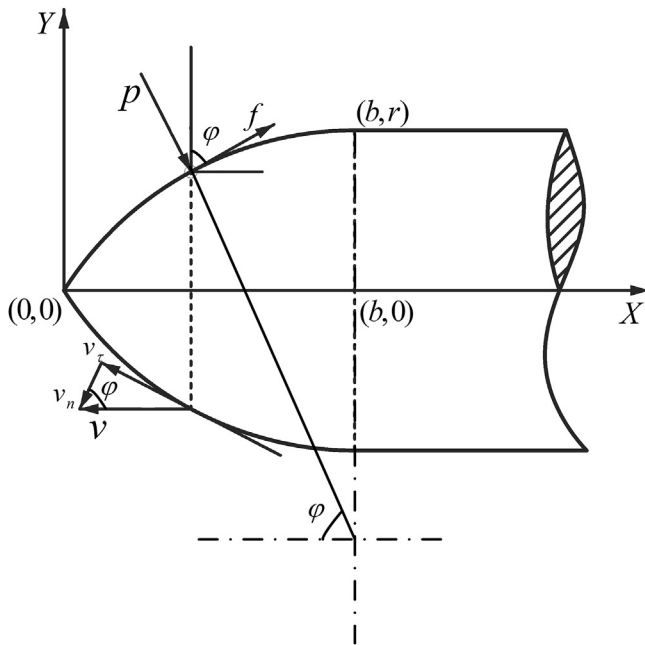**Fig. 1.** Normal penetration process with ogival nose projectile.

Fig. 2. Cross-section of an axisymmetric penetrator.

conductivity of projectile material, is usually at micron scales. Regarding the heat converted from plastic work, it is a common phenomenon in the high strain-rate plastic deformation. The thermal softening will lead to instability of mechanical properties and hence the failure of the material. Due to the different relative sliding velocity and stress state in different locations of the projectile, the temperature rise derived from these two generation mechanisms varies significantly, resulting in the different distribution of mass loss and eventually nose blunting of the projectile.

2.2. Discretization and fundamental assumptions

In order to deal with the penetration process with high nonlinearity, a discrete 2D model is established to calculate the distribution of the temperature rise, as shown in Fig. 3. With the coordinates *X-Y* fixed on the projectile, the original projectile is divided into (nj-1) sticks along the *Y* axis with each width of stick as l_c. Herein we have $r=(nj-1)*l_c$. The left shape of the stick depends on the original nose contour of the projectile shown in dotted lines in Fig. 3. In particular, the wedge angle θ_j is formed in the discretization of the projectile, herein $\theta = \pi/2-\varphi$. The subscript j ($1 \leq j \leq nj$) denotes the sequence number in the spatial discretization along the *Y* direction. Meanwhile, by dividing the total time of the tunnel stage into ni parts with each time step Δt, the iterative calculation is established to obtain the final shape of the projectile. The superscript i ($1 \leq i \leq ni$) denotes the ith time step in the temporal discretization of the tunnel stage, as shown in Fig. 4. There are some assumptions that must be followed to carry out the iterative calculations:

(1) The projectile retains axial-symmetrical during the whole penetration process. The mass loss occurred on the surface of the projectile also remains axial-symmetrical during the tunnel stage. Therefore, the three-dimensional problem can be simplified into a two-dimensional receding model, shown in Fig. 3.

(2) The discrete points move in the coordinates of *X-Y*. As shown in Fig. 4, the jth discrete point (x_j^i, y_j^i) of the nose surface at the time t^i recedes along the X axis to the point (x_j^{i+1}, y_j^{i+1}) at the next time t^{i+1}.

(3) The surface geometry of the projectile and the surface stress stay constant during each time step Δt. The movements of the discrete points take place at the end of the time step after determining the receding displacement.

(4) The density and the related thermal properties of the projectile and the concrete target remain unchanged during the
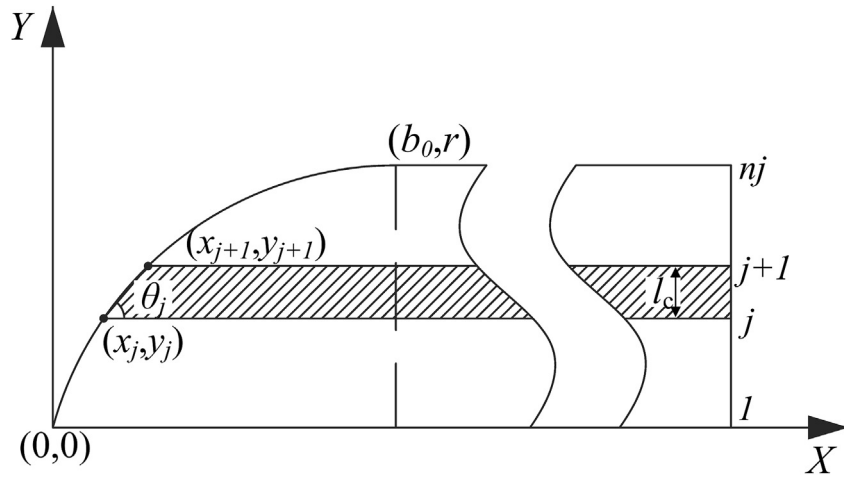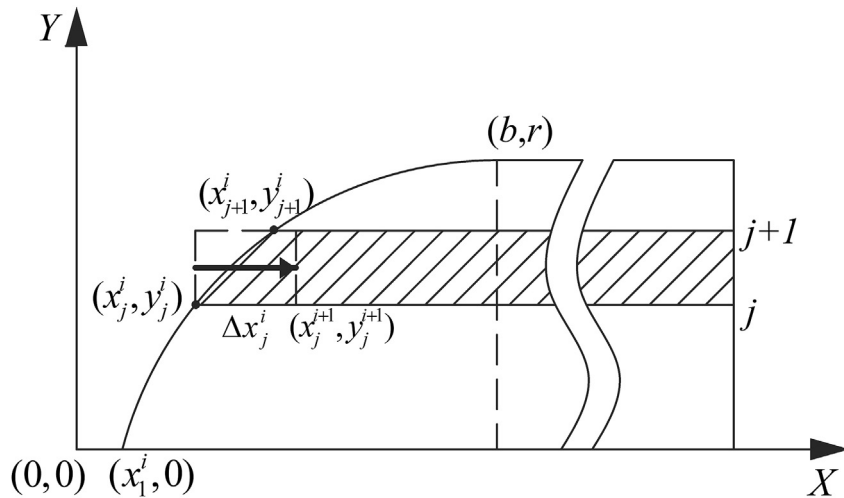
Fig. 3. Discretization of the projectile at initial time.

Fig. 4. The receding model of the projectile at time t^i.

penetration. The mass loss only comes from the projectile shape variation, without the consideration of the embedded concrete particles. The material of the projectile is supposed to be homogeneous.

Based on the discussions and assumptions above, the nose sharp variation of the projectile can be represented by the movements of the discrete points during the penetration process. The two modes of heat generation and the corresponding failure criteria are to be further analyzed in the following sections.

2.3. Frictional heat generation and conduction

As a classic physics problem, heat generated by friction has been investigated theoretically in the low velocity impact range from micro to macro-scale (Rigney et al., 1984; Rigney and Hirth, 1979; Krafft, 1955). However, surface friction subjected to high velocity sliding is quite different from that, due to the time-dependence of the rate of heat transfer. The phenomena, such as phase transformation, large localized deformations as well as melting occurred in the friction process make the theoretical description complex (Bowden and Persson, 1961; Montgomery, 1976). Concentrated in the thin region of the exterior layer of the material within a short duration of time, the temperature rise, namely "flash temperature"

(Blok, 1963; Archard, 1959), will reach and further exceed the melt point during the high speed cutting of metallic materials. Jones et al. (2002b); Jones and Rule, 2000). conducted investigations on the dynamic friction coefficient or the resistance force of an ideal rigid projectile based on the linear velocity-dependent friction. However, the temperature distributions generated by friction and heat conduction still remain to be investigated.

In analyzing the temperature rise distribution induced by high velocity friction, a representative interaction model between the projectile and the concrete is taken from the entire discrete model in Section 2.2. As shown in Fig. 5, the projectile stick moves to the concrete in $-X_n$ direction at a velocity of v, leading to the uniform heat generation in the contact interface AB due to the relative sliding velocity. The distribution of temperature rise due to sliding friction is estimated based on the following assumptions:

(1) No deformation is considered in the infinitesimal time interval. Regarding the projectile as a rigid body during the time interval Δt, so that the heat generated at the projectile/target interface is conducted into both the projectile and concrete.

(2) The sliding velocity and the coefficient of friction are considered constant. Ignore the influence of the resistance force on the velocity of the projectile during the time interval Δt. A fixed value of coefficient of friction in Eq. (4) is
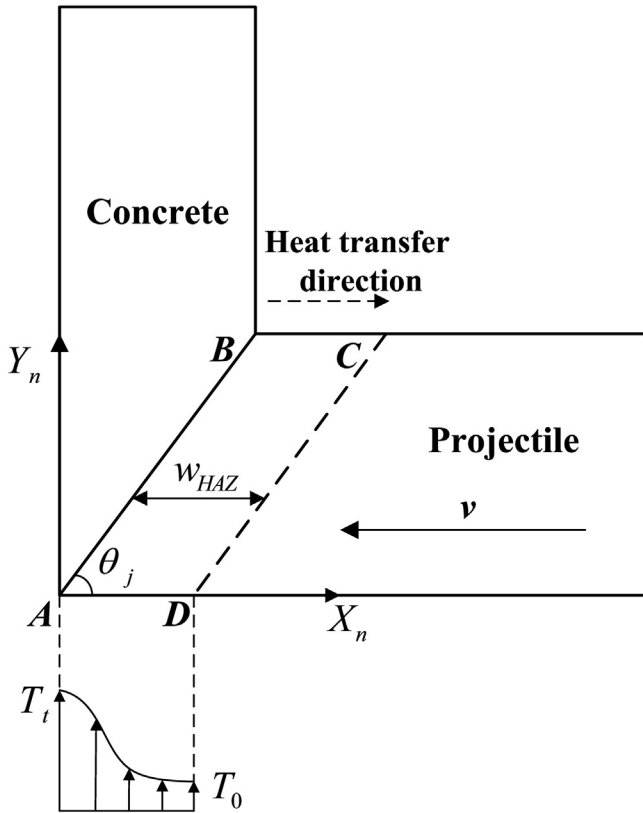
Fig. 5. One-dimensional coordinate system of the heat generation by the surface friction between the *j*th stick of the discrete projectile and the concrete.

considered without accounting for the dynamic friction in order to obtain the simplified analytical solutions of the temperature distribution on the projectile.

(3) One-dimensional heat conduction is considered. There is only a horizontal thermal conduction along the X_n axis from interface *AB* to interface *CD*, shown in Fig. 5. Heat conduction from the adjacent sticks of the discrete projectile is neglected.

Based on the assumptions mentioned above, the one-dimensional heat conduction in each side of the penetration system can be expressed by the following equations.

The projectile side

$$\rho_p c_p \frac{\partial T_t}{\partial t} = k_p \frac{\partial^2 T_t}{\partial X_n^2} \tag{5}$$

The concrete side

$$\rho_c c_c \frac{\partial T_t}{\partial t} = k_c \frac{\partial^2 T_t}{\partial Y_n^2} \tag{6}$$

where ρ, c and k are density, specific heat capacity and heat conductivity respectively, and the subscript p and c refer to the projectile and the concrete target. As the uniform frictional heat generated at the projectile/concrete interface *AB* is conducted at both sides, the boundary conditions of the projectile and the concrete at the interface *AB* ($X_n = 0$) can be therefore expressed as:

$$Q_p = -k_p \frac{\partial T_t}{\partial X_n} \tag{7}$$

$$Q_c = -k_c \frac{\partial T_t}{\partial Y_n} \tag{8}$$

$$Q = Q_p + Q_c \tag{9}$$

where Q is the rate of heat generation by friction per unit area and has the expression as:

$$Q = f v_\tau \tag{10}$$

where v_τ is the relative sliding velocity between the projectile and the concrete.

Assuming the micro asperities shearing by the friction, a thermodynamic model involved with plastic deformation and melt of material was developed by (Klepaczko and Hughes(2005), Klepaczko (2001). to estimate the coefficient of friction under high speed sliding. Thus a simplified estimation of the width of the heat effected zone (HAZ) (Klepaczko and Hughes, 2005; Klepaczko, 2001) is proposed with diminishing the effect on the area far away from the contact interface. Here, ten times of the width of the HAZ is taken as the other boundary for the heat transfer calculation:

$$w_{HAZ} = \frac{10}{\alpha} \left(\frac{k_p L_p}{\rho_p c_p v} \right)^{1/2} \tag{11}$$

in which constant α is estimated as $\alpha = 1/(2\pi)^{0.5}$, L_p is the length of the projectile. Since there is no heat flux across the surface at this point, the boundary condition at $X_n = w_{HAZ}$ is expressed as:

$$\frac{\partial T_t}{\partial X_n} = 0 \ T_t(X_n, 0) = T_0 \tag{12}$$

where T_0 is the initial temperature ($T_0 = 298$ K).

Therefore, depending on the impact condition and the related thermal parameters, the distribution of the temperature rise on the exterior of the projectile is derived by combing Eqs. 5–12.

2.4. Temperature distribution in adiabatic shear band

The phenomenon of adiabatic shear is known as one of the most important failure mechanisms during explosive and high velocity penetration. The formation of adiabatic shear banding (ASB) is a result of the highly coupled competition between thermal softening and the strain or strain rate hardening mechanisms (Zener and Hollomon, 1944; Clifton et al., 1984; Bai, 1982; Molinari and Clifton, 1987). Coupled with high temperature, pressure and strain-rate at the interface between the projectile and the concrete, highly localized plastic deformations occur due to the material failure during the high velocity penetration. The stress imposed on the penetrator will greatly exceed its strength during the contact in the penetration process. Different from the penetration into armor by a shaped charge jet or the armour-piercing kinetic energy weapons, mass loss or the plastic flow only appears on the surface of the projectile's nose during penetrating concrete. However, the metallurgical structure of the inner matrix remains unchanged as the temperature gradient diminishes sharply along the depth of the surface of projectile. The effect of thermal softening, converted mostly from plastic work, will quickly result in the thermoplastic instability when the thermal softening effect exceeds the strain hardening effect under high strain-rate, which has been verified experimentally by Magness (1994). The thermodynamics characteristics of the material are the key determinant of the penetration capabilities of a projectile (Rosakis and Ravichandran, 2000). An accurate assessment of the temperature rise in the plastic

deformation zone is of crucial importance in understanding the thermo-mechanical instability during penetration with mass loss.

Similar to the analysis of the temperature distribution by sliding friction, a representative local contact separated out from the entire discrete model in Section 2.2 is investigated using the ASB theory, as shown in Fig. 6. The temperature induced by plastic deformation is calculated under the following assumptions:

(1) Plane strain conditions. The axial symmetric projectile and moss abrasion ensure that plane strain deformation conditions are maintained during the entire penetration process.
(2) In the area of ASB, the shear stress, strain and temperature fields depend only on the coordinate $X_{\tau n}$.
(3) Heat conduction in the ASB is not considered. The temporal scale of the shear deformation is much shorter than that of the heat conduction, so that most of the generated heat keeps inside the ASB zone.
(4) Constant thickness of the ASB w_{ASB}. The thickness of the ASB is supposed to be constant in order to simplify the analytical derivation.

With the combined effect of pressure and shear, as shown in Fig. 7, the similar physical phenomena occurred in metal cutting has been discussed theoretically by Oxley and Hastings (1977) and Tounsi et al. (2002). A typical shape of the primary shear zone was defined to evaluate the plastic deformation during cutting. The analytical distribution of the effective strain-rate along the depth of ASB should obey the following equations according to the experimental measurement and numerical validation:

$$\dot{\bar{\varepsilon}} = \dot{\bar{\varepsilon}}_{AB}\left(1 - \frac{x_{\tau n}}{w_{ASB}}\right)^{p^*} \quad \text{for } x_{\tau n} \subseteq [0 : w_{ASB}] \tag{13}$$

where $\dot{\bar{\varepsilon}}_{AB}$ represents the effective strain rate at the contact shear plane AB, $x_{\tau n}$ is the coordinate value related to the thickness of the

Fig. 6. Formation of the ASB by the contact between the jth stick of the discrete projectile and the concrete.

ASB, i.e. w_{ASB}. The parameter p^* is a constant depending on the projectile material. Here, $p^* = 4$ is taken for the most common projectile material 4340 steel.

Consequently, the effective strain in the ASB zone is obtained from the time integration of the effective strain rate:

$$\bar{\varepsilon} = \int_0^t \dot{\bar{\varepsilon}} dt \tag{14}$$

Intensive plastic deformations of the projectile material occur on and near the contact surface during the sliding contact, which is a very complicated process related to the sliding velocity, normal pressure, etc. The microstructure change of surface topography, phase transition occurred will affect the friction coefficient and the properties of the material locally. Metallographic observations and measurements (Fleck et al., 1994; Heilmann and Rigney, 1981) were conducted to obtain the qualified strain distribution along the depth from the contact surface. However, there are rare experimental data existed that address the contact between the steel and the concrete. The maximum effective strain can be derived approximately from the similar law for the friction between the high strength alloy steel and concrete, which will be validated later by experimental penetration results.

$$\bar{\varepsilon}_{AB} = e^{\left(\frac{k_1 v_t}{G}\right)^{k_2}} \tag{15}$$

where G is the shear modulus of the projectile material, k_1, k_2 are material constants, which are closely related to the properties of the materials in contact, especially the thermo-mechanical parameters.

As one of the most widely used material constitutive equation for thermodynamic process, the visco-plastic Johnson-Cook constitutive model (Johnson and Cook, 1983) is employed to obtain the analytical temperature distribution in the ASB zone. The flow stress σ can be expressed as a function of the effective plastic strain $\bar{\varepsilon}$, the effective strain rate $\dot{\bar{\varepsilon}}$, and the temperature T.

$$\sigma = (A + B\bar{\varepsilon}^n)\left(1 + C\ln\frac{\dot{\bar{\varepsilon}}}{\dot{\varepsilon}_0}\right)\left(1 - \left(\frac{T - T_0}{T_m - T_0}\right)^m\right) \tag{16}$$

where $\bar{\varepsilon}_0$ is the reference strain rate, which is taken as $1\,s^{-1}$. T_0 is the room temperature. T_m is the melting temperature of the projectile material. A, B, C, n and m are material constants.

Converted from plastic deformation process, the temperature rise in the ASB zone in the exterior surface of the projectile nose can be expressed as (Wang, 2006):

$$T_a = \frac{\beta}{\rho_p c_p} \int \sigma d\bar{\varepsilon} \tag{17}$$

where β is the work to heat conversion factor. Combining Eqs. 14–17, the distribution of temperature gradient in the ASB zone with the maximum value located on the contact interface can be obtained.

2.5. Failure criteria of the plasticity instability

The onset criterion for the ASB growth and propagation is a major issue to evaluate the dynamic failure mode of the ductile material. Systematic investigations and discussions (Bai and Dodd, 1992; Wright, 2002; Schoenfeld and Wright, 2003; Zhou et al., 1996; Li et al., 2001) have been conducted on the dynamic ASB formation, indicating that the susceptibility of the material to
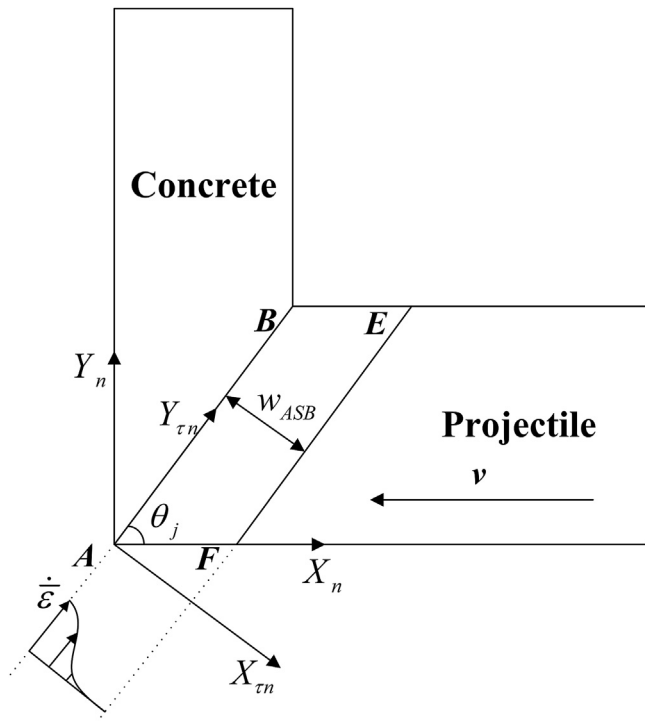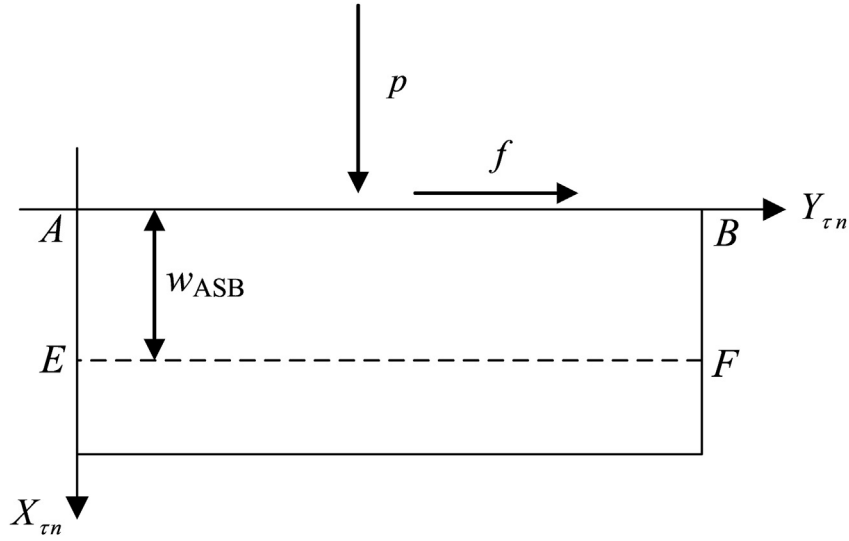
Fig. 7. Stress condition of the surface of the discrete projectile.

plasticity instability depends on factors such as heat capacity, heat conductivity, microstructure, defects and strain-rates etc. The undergoing physical process such as dynamic recrystallization and microstructure reformation inside an ASB should be modeled by the failure criterion. Based on the assumption that mass loss caused by heat virtually all comes from the friction (Section 2.3) and the plastic work converted (Section 2.4), the failure of a viscoplastic material will occur when the local temperature beyond the crucial one specified by the criterion. A temperature-based ductile failure criterion for the ASB propagation is proposed by Medyanik et al. (2007) to simulate the initiation and propagation of the dynamic adiabatic shear bands. The failure criterion is expressed as:

$$T_{cr} = T_{DRX} + (T_m - T_{DRX})\frac{\dot{\varepsilon}_{DRX}}{\dot{\varepsilon}_{DRX} + \dot{\bar{\varepsilon}}} \tag{18}$$

where T_{DRX} is the minimum temperature at which the phase transformation process, i.e., dynamic recrystallization takes place in the ductile material under high temperature, high strains and high strain rates. The parameter $\dot{\varepsilon}_{DRX}$ is the value of strain rate when the dynamic recrystallization begins to play an important role in the deformation mechanism. Apparently, the critical temperature T_{cr} decreases with the increase of effective strain-rate $\dot{\bar{\varepsilon}}$. As shown in Fig. 8, there exists a transitory stage between the transformation temperature T_{DRX} and the melting temperature T_m, in which the critical temperature T_{cr} approaches T_{DRX} when the stain-rate grows to infinity and approaches T_m as the strain-rate approaches zero.

As discussed in Section 2.1, a quantitative assessment of the temperature rise in the surface layer of a projectile should fully take into account of the two modes of heat generation. The quantitative result of the temperature from friction (T_t (X_n,t)) and plastic deformation (T_a ($X_{n\tau}$, t)) can be obtained from Eq. (7) and Eq. (17). The distribution of temperature along the depth of surface of projectile can be obtained by adding the temperature together at any time during the penetration process, ignoring the mutual influence. Therefore, the total temperature rise is determined by the total energy obtained from the superposition of individual energy values. The total temperature (T_{total} (X_n,t)) is a function that depends on the position of depth and time. Meanwhile, the critical temperature T_{cr} (X_n,t) for each discrete unit of the projectile can be determined by its stress condition from Eq. (18). Combing the temperature calculation derived from surface friction and heat converted from plastic work, the failure areas can be determined

when compared the sum distribution of the temperature T_{total} ($=T_t + T_a$) with the critical temperature T_{cr}. The discrete points of the projectile surface move to the new position, resulting in blunting of the ogival nose of the projectile.

3. Iterative calculations of the mass abrasion model

Utilizing the spatial discretization of the projectile and the assumptions made previously, the two modes of heat generation in the projectile during the tunnel stage can be calculated quantitatively. The thermo-mechanics penetration process including mass loss can be decoupled with the movement of the projectile and the movement of the discrete points. According to the temperature-based ASB failure criterion, the receding displacement of each discrete point can be obtained during each time step Δt, resulting in the variation of the nose shape of projectile.

Based on the equation of uniformly accelerated motion and the previous assumptions, the parameters describing movement of the projectile at the time t^i can be expressed as:

$$v^i = v^{i-1} + a^{i-1}\Delta t \tag{19}$$

$$a^i = F_x^{i-1} / M^{i-1} \tag{20}$$

$$\Delta z^i = v^{i-1}\Delta t + a^{i-1}\Delta t^2 / 2 \tag{21}$$

where a, v and M are the acceleration, velocity and the mass of the projectile, respectively. The parameter F_x is the resistant force on the nose of projectile along the X axis. Δz is the displacement of the projectile during the time step Δt from the time t^{i-1} to t^i. To guarantee the stability and smoothness of the iterative calculations, the time step Δt has to be set appropriately (on μs scale). Inappropriate time step will lead to the unconvergence of the results. Herein,

$$\Delta t \leq \frac{n_{tHAZ}c_p\rho_p}{2k_p}\left(\frac{w_{HAZ}}{n_{xHAZ}}\right) \tag{22}$$

where n_{xHAZ} is the discrete number of the HAZ in the finite difference calculation. n_{tHAZ} is the discrete number of each time step Δt.

As the cavity expansion velocity and the relative velocity depend on the velocity of the projectile, the following relations exist.
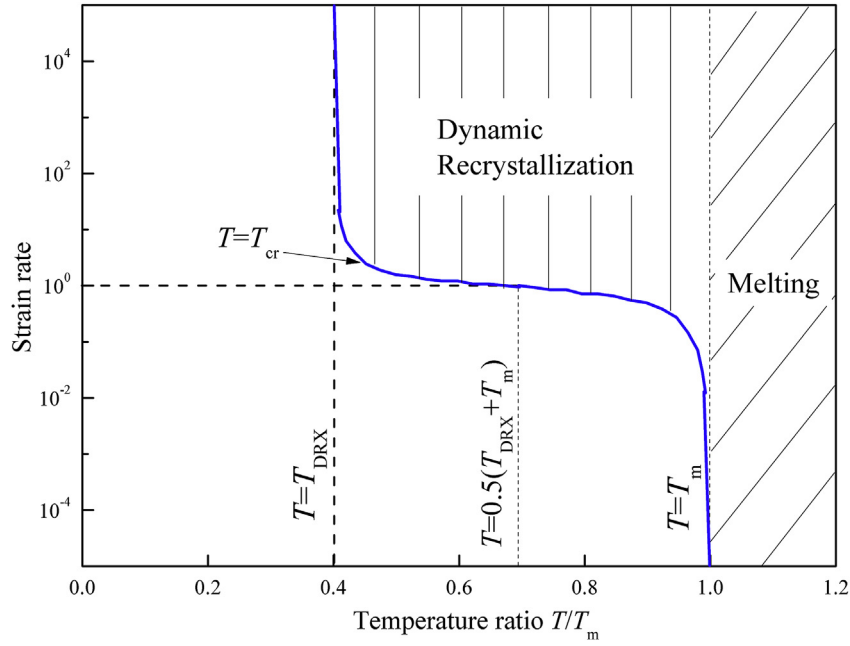
Fig. 8. Failure criterion responding to strain rate and temperature (Medyanik et al., 2007).

$$v_{nj}^i = v^i \sin\left[\left(\theta_j^{i-1} + \theta_{j-1}^{i-1}\right)\big/2\right] \tag{23}$$

$$v_{\tau j}^i = v^i \cos\left[\left(\theta_j^{i-1} + \theta_{j-1}^{i-1}\right)\big/2\right] \tag{24}$$

$$\theta_j^i = \arctan\left[\left(y_{j+1}^i - y_j^i\right)\big/\left(x_{j+1}^i - x_j^i\right)\right] \tag{25}$$

Based on the analyses above, the total temperature rise is contributed by the friction heat T_t and the heat converted from plastic work T_a, as discussed in Section 2.3 and Section 2.4. For the *j*th stick (the interval between y_j^i and y_{j+1}^i) of the discrete projectile in the spatial discretization, the total temperature distribution related to axis X_n along the stick at the time t^i can be expressed as

receding displacement Δx_j^i can be determined by comparing the total temperature distribution with the critical temperature for each stick of the discrete projectile. The discrete points move to the area where the temperature is below the critical value. The displacement of the discrete points at the time t^i can be expressed as

$$x_j^i = x_j^{i-1} + \Delta x_j^i \tag{27a}$$

$$y_j^i = y_j^{i-1} \tag{27b}$$

Then the mass loss caused by the receding movement of the discrete points can be further expressed as the mass change of the finite circular tables, around the axis of the projectile.

$$\Delta M^i = \sum_j \Delta M_j^i = \sum_j \rho_p\left(V_j^i - V_j^{i-1}\right)\frac{\pi\rho_p}{3}\sum_j\left[\begin{array}{c}\left(y_{j+1}^{i-12} + y_{j+1}^{i-1}y_j^{i-1} + y_j^{i-12}\right)\left(x_{j+1}^{i-1} - x_j^{i-1}\right)\\-\left(y_{j+1}^{i2} + y_{j+1}^i y_j^i + y_j^{i2}\right)\left(x_{j+1}^i - x_j^i\right)\end{array}\right] \tag{28}$$

$$T_{total_j}^{\ i}(X_n) = T_{t_j}^{\ i} + T_{a_j}^{\ i} \tag{26}$$

According to the ASB-based temperature failure criterion, the

Thus the instant mass of the projectile at time t^i is $M^i = M^{i-1}-\Delta M^i$. On the other hand, the resistance force at the time t^i on the nose of the projectile is the sum of the force exerted on the side area of the finite circular tables, expressed as

$$F_x^i = \int_S (p\sin\theta + f\cos\theta) = \sum_j\left[\begin{array}{c}\left(\dfrac{p_j^i + p_{j+1}^i}{2}\right)\dfrac{y_{j+1}^i - y_j^i}{L_j}\left(\pi y_j^i L_j + \pi y_{j+1}^i L_j\right)\\+\left(\dfrac{f_j^i + f_{j+1}^i}{2}\right)\dfrac{x_{j+1}^i - x_j^i}{L_j}\left(\pi y_j^i L_j + \pi y_{j+1}^i L_j\right)\end{array}\right] = \dfrac{\pi}{2}\sum_j\left[\begin{array}{c}\left(p_j^i + p_{j+1}^i\right)\left(y_{j+1}^i 2 - y_j^i 2\right)\\+\left(f_j^i + f_{j+1}^i\right)\left(y_{j+1}^i + y_j^i\right)\left(x_{j+1}^i - x_j^i\right)\end{array}\right] \tag{29}$$

where the integration interval S is the area of the nose, which can be transformed to accumulation of the normal and tangential stress on each discrete stick along the X axis.

The mass loss penetration model can be further solved by the finite difference method. The shape variation of the projectile is analytically represented with this incremental method, as shown in Fig. 9. Apparently, the iterative calculations will stop until the instant velocity v reaches zero.

4. Validation of theoretical predictions with experimental results

The influence of significant mass loss on the terminal lethality subjected to high velocity penetration has been investigated experimentally. The mass loss iterative model proposed above is validated with the experimental data provided by Forrestal et al. (1996). This includes the percentage of mass loss, the final depth
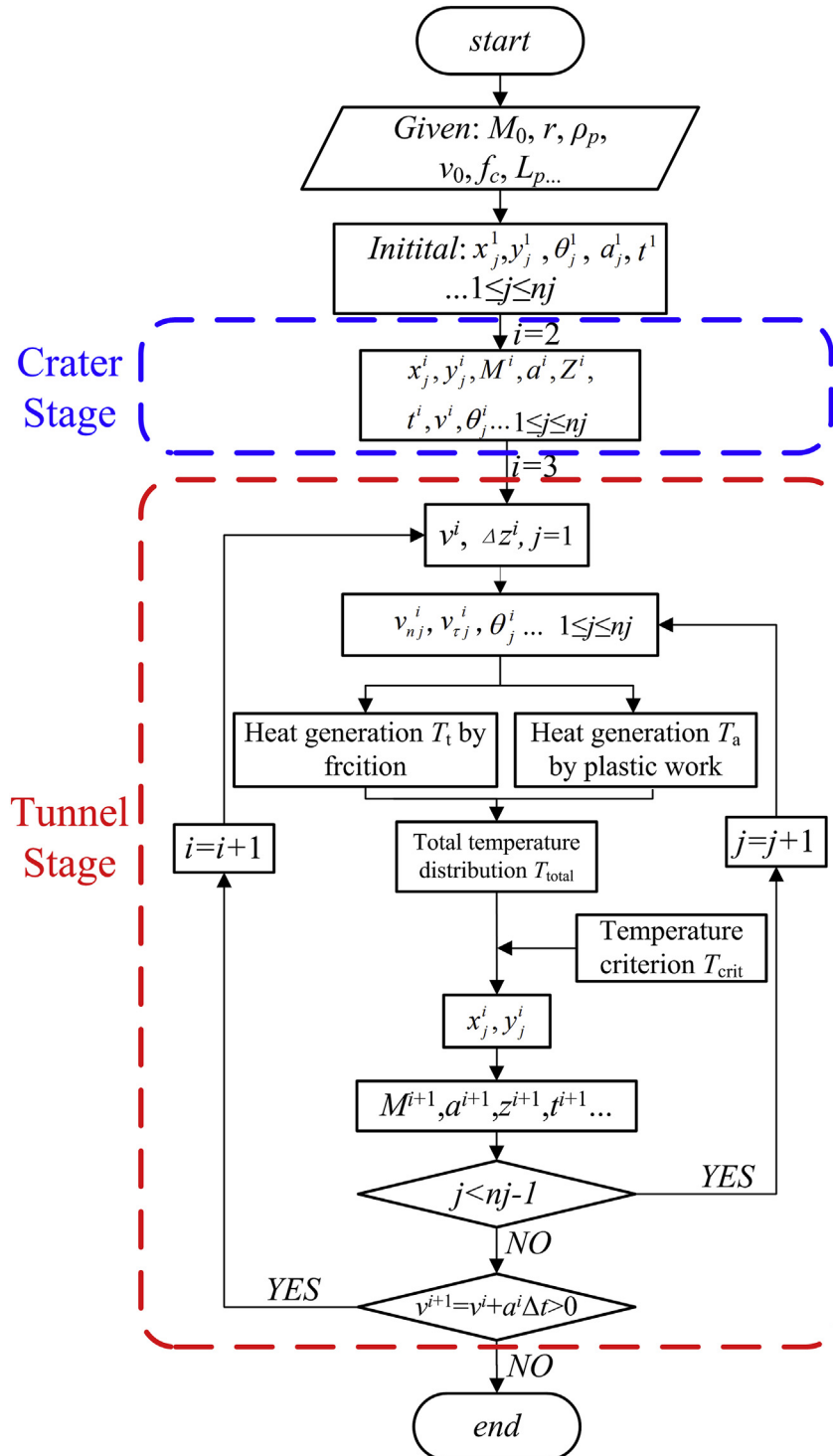

Fig. 9. Flow chart of the iterative calculation.

of penetration and the residual shape of projectile. The experimental conditions of the projectiles and targets are listed in Table 1. Focused on the thermodynamic analysis of the projectile, the parameters of concrete are fixed, ignoring the influence of difference concrete components. The relevant thermodynamic parameters used in the calculation are shown in Table 2.

The calculated residual shapes and the length subjected to different initial impact cases are compared with the recovered projectiles from the tests, as shown in Figs. 10–13. The corresponding residual length of projectiles L_p from the iterative model are listed on the right. Clearly, the nose of the projectiles becomes blunter with the increase of the impact velocity. Approximately, the predictions from the iterative calculations correlate well with the experimental data to some degree. It appears that the predicted nose shapes remain pointed, compared with the experimental post-test projectiles. The possible reason for the deviation was caused by the complexity of failure modes for the material of projectile during the penetration process. The thermodynamic mass abrasion proposed could not predict the bending or fracture as well as the other structure responses of the projectile. The mass loss model included with multiple failure modes for the high velocity penetrator will be studies in the future work.

Furthermore, to help understand the underlying differences of the high-speed penetration with the effect of mass loss, especially the physical parameters that cannot be measured experimentally, the predicted mass loss and the experimental results for Case 1 are compared in Table 3. Clearly, severe mass loss has occurred when the impact velocity is increased from 545 m/s to 1201 m/s, which agrees well with the corresponding experimental data. By setting the receding distance Δx^i_j in Eq. (27a) as zero, the calculations without mass loss, i.e. the rigid penetration, are also listed in Table 3, demonstrating the great influence of the effect mass loss on the DOP of the projectile in the high-speed penetration.

Fig. 14(a)-(d) show the time histories of the characteristic parameters derived from the iterative calculations respectively, including the percentage of mass loss ($\gamma = \Delta M/M_0$), the deceleration (a), the dimensionless depth of penetration (z/d) and the dimensionless shape-related parameter (b/d). It is clearly shown in Fig. 14(a) that the mass loss happening in the tunnel stage is velocity-dependent, that is to say, the maximum mass loss rate ($\Delta M/\Delta t$) occurs at the start of the tunnel stage and gradually decreases to zero at the end of the penetration process. On the other hand, based on the theoretical results in Fig. 14(b), it is reasonable to conclude that the maximum deceleration appears at the beginning of the tunnel stage and increases with the impact velocity. However, a special phenomenon, defined as the "secondary peak" deceleration, appears during the tunnel stage, which is marked out in Fig. 14(b). With a higher value and lagged occurrence time, the "secondary peak" deceleration subjected to the velocity of 1201 m/s is distinctly different from that of the low velocity cases. As a result of the mass loss effect, the structural integrity and the stability of the charge of the projectile subjected to high velocity penetration need to be reassessed by weapon designers. However, it is very difficult to obtain the real-time physical parameters in experiments due to the lack of high-velocity launch for the projectile with large diameter. Meanwhile, the signal acquisition of the sensor embedded in the projectile remains a challenge in this high velocity penetration experiments. There exists rarely study published to address this issues. As shown in Fig. 14(c), the dimensionless depth of penetration (z/d) increases as increasing the impact velocity due to the assumption of straight penetration trajectory. Regarding Fig. 14(d), the parameter b/d is employed to quantitatively describe the variation of the instant nose shape during penetration. Clearly, the final value of b/d tends to 1.1 with the increasing of impact velocity.

4.1. Further analysis on the high-speed penetration with mass loss

Theoretical analysis and experimental observations have confirmed the significant influence of mass loss and nose abrasion on the performance of the KE projectile subjected to high velocity penetration. Primarily involved with the thermoplastic instability, material flow and abrasive wear, the severity of mass loss is closely related to the several influential factors, including initial impact conditions, thermodynamic parameters related to the penetrator and the strength of the target, etc. Therefore, further analyses on the mass loss during high velocity penetration are conducted on the basis of the incremental mass loss model.

4.2. The critical velocity v_c of the mass loss

Since the mass loss occurs in the tunnel stage, it is reasonable to infer that the instant velocity is possibly a dominant factor for the penetration into a semi-infinite concrete target. With further analyzing the time history of the mass loss and the velocity in the entire penetration process of Case 1, as shown in the lower half of Fig. 15, it indicates that there exits a time region in which almost no mass loss occurs with the penetration going on. The beginnings of the time period are associated with the corresponding velocity-time curves in Fig. 15. The velocity is found to be almost the same level ($v_c = 225$ m/s) that the projectile presents to be rigid when the instant velocity is below this critical velocity v_c at the later stage of the penetration process.

It can be inferred on the basis of the failure criterion that the

Table 1
Experimental conditions of four penetration events for ogival projectile (Forrestal et al., 1996).

	Case 1	Case 2	Case 3	Case 4
Projectile				
Material	4340 steel	4340 steel	4340 steel	4340 steel
M_0 (kg)	1.6	0.478	0.064	0.064
d (mm)	30.5	20.3	12.9	12.9
Ψ	3	3	3	4.25
ρ_p (kg/m^3)	7850	7850	7850	7850
L_p/d	10	10	6.88	6.88
Targets				
Material	Concrete	Concrete	Grout	Grout
f_c (MPa)	51	62.8	13.5	21.6
ρ_c (kg/m^3)	2300	2300	2000	2000
Agreegate material	Quartz	Quartz	Quartz	Quartz
Moh's hardness of aggregate	7	7	7	7

Table 2
List of the relevant parameters associated with iterative calculation (Wang, 2006; Forrestal et al., 1988; Campbell et al., 1991).

A (MPa)	B (MPa)	C	n	m	T_0(K)	T_m(K)	w_{ASB}(μm)
792	510	0.014	0.26	1.03	298	1793	300

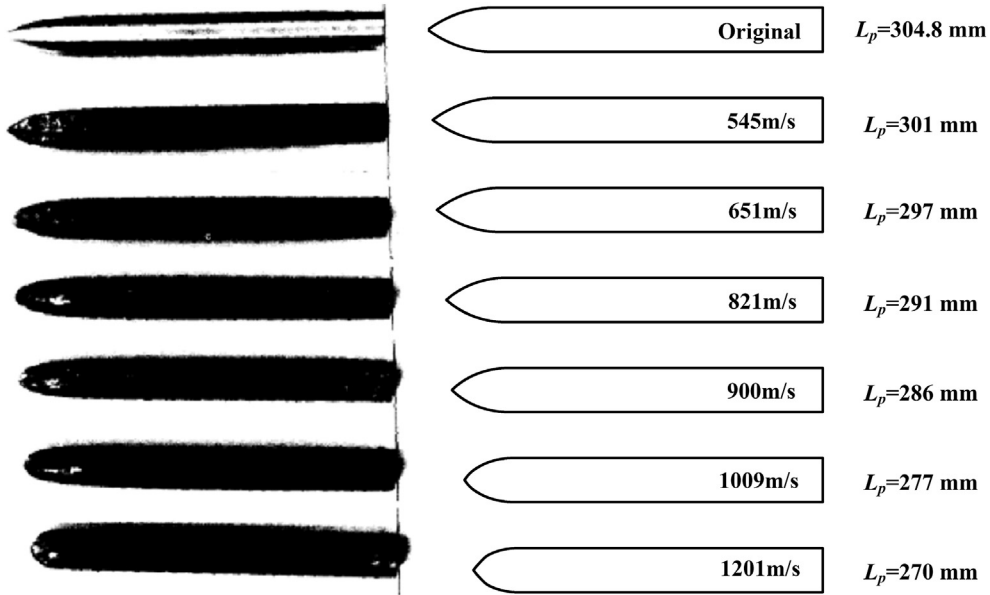| k_p (W/(m·K))	c_p (J/(kg·K))	k_c (W/(m·K))	c_c (J/(kg·K))	β	μ	k_1 (MPa·s/m)	k_2
44.5	477	1.65	880	0.9	0.01	1.05	0.5

Fig. 10. Comparison of residual projectile shape for Case 1.
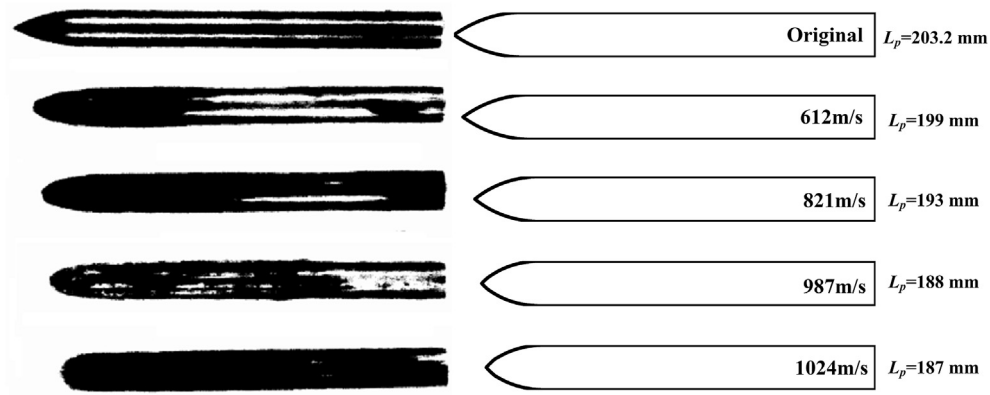

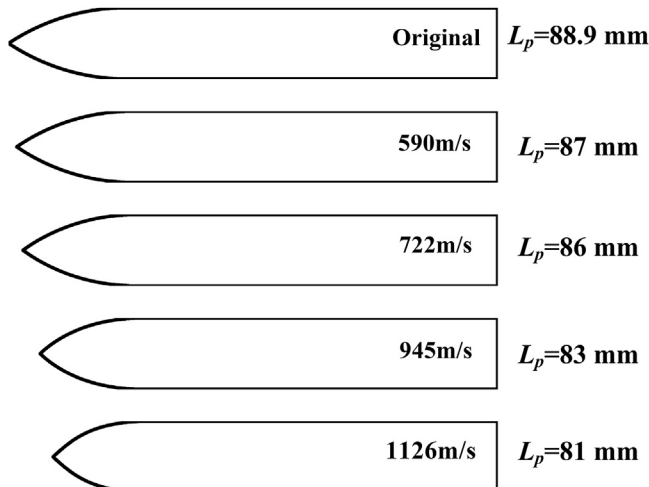**Fig. 11.** Comparison of residual projectile shape for Case 2.

Fig. 12. Residual projectile shape from iterative calculations for Case 3.

critical velocity is closely depended on the interactions between the projectile nose and the target medium at that moment, the thermoplastic property of the projectile as well as the compressive strength of the concrete. A practical linear relationship between the total percentage of the mass loss and the initial kinetic specific energy of the projectile was proposed by Silling and Forreatal (2007) by fitting the experimental data. Based on the critical velocity proposed above, the relationship is further modified as follows:

$$\gamma = \begin{cases} 0 & v_0 \leq v_c \\ \dfrac{\Delta M}{M} = \dfrac{1}{2}C'\left(v_0^2 - v_c^2\right) & v_c \leq v_0 \leq v_p \end{cases} \tag{30}$$

where C' is an empirical constant. v_p is the transition point from nondeformable projectile penetration regime to semi-hydrodynamic penetration regime (Chen and Li, 2004), which will be analyzed later. No mass loss occurred when the impact velocity is below the critical velocity v_c. The modified linear relationship is appropriate for the nondeformable penetration regime in which the projectiles maintain the structural integrity.

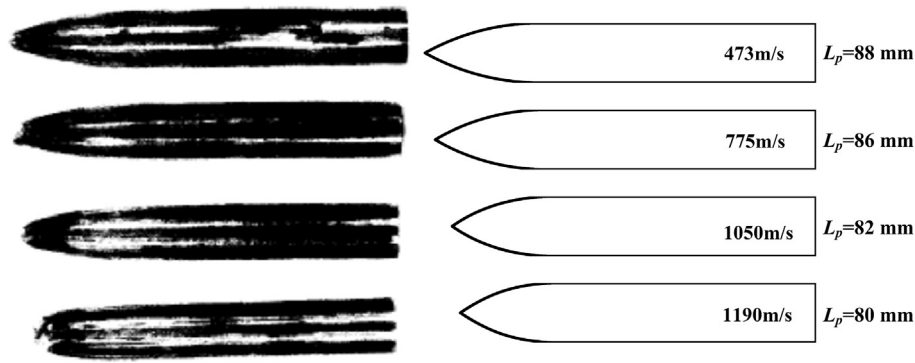Here, the valid range of the modified formula is determined by

Fig. 13. Comparison of residual projectile shape for Case 4.

Table 3
Comparison between the theoretical calculations and experimental results.

Impact velocity/(m/s)	DOP (m)			Mass loss (%)	
	Experimental results (Forrestal et al., 1996)	Calculations without mass loss model	Calculations with mass loss model	Experimental results (Forrestal et al., 1996)	Calculations with mass loss model
545	0.56	0.62	0.61	2.0	1.3
651	0.78	0.85	0.83	3.1	2.23
821	1.23	1.26	1.22	4.4	4.2
900	1.41	1.48	1.40	5.4	5.3
1009	1.75	1.78	1.63	6.4	6.5
1201	2.03	2.34	1.97	6.8	9.2

the critical velocity v_c and the upper limit velocity v_p. Further investigations reveal that the other penetration events in Table 1 have the similar situation. Different theoretical critical velocity can be derived for different impact Cases by utilizing the mass loss iterative model above. Meanwhile, as shown in Fig. 16, the linear fitting between the initial kinetic energy and the mass loss for four penetration events are conducted without the consideration of the high-speed results, which is beyond the valid range v_p. Table 4 lists the comparisons between the linearly fitted values of v_c and the predictions from the mass loss iterative calculations. Clearly, the theoretical predictions of the critical velocity agree with the fitted experimental data, indicating the existence of the critical velocity for mass loss during the penetration. Moreover, the linear fitting values of C' for different penetration Cases are also listed in Table 4.

4.3. The "secondary peak" deceleration

Involving with high temperature, high pressure and high strain-rate, physical phenomena such as thermal softening, material plastic flow, nose abrasion and eventual mass loss will happen during the high velocity penetration. It is well known that the blunt projectile nose generates larger drag force, resulting in significant change on the evaluation of key technologies used in the EPW, such as the fuze safety.

It is indicated from Fig. 14(b) that the deceleration of the low velocity penetration has its maximum value at the beginning of the tunnel stage and decreased gradually until it is stopped, which is similar to the rigid penetration analyzed by Chen and Li (2014). Comparatively, the deceleration subjected to the velocity of 1201 m/s in Case 1 will increase distinctly at the beginning of the tunnel stage and then decrease gradually when the mass loss effect is taken into account. It can be inferred that the occurrence of the "secondary peak" deceleration is mainly ascribed to the change of

the nose shape caused by mass loss. Based on the iterative calculation, further analyses are conducted on the deceleration pulse subjected to higher impact velocities. As shown in Fig. 17, distinct vibrations of deceleration are shown in the beginning of the tunnel stage. The duration and amplitude of the vibration increase with the enhancement of impact velocity, resulting in the extreme adverse condition for the high-speed projectile.

It can be inferred that the corresponding transition velocity v_s, when the "secondary peak" deceleration appears, should be the key upper limit for the application of the EPW. In other words, the enhancement of the initial impact velocity beyond this transition point will aggravate the extent of mass loss of the projectile, resulting in the structure failure and dramatic decrease of the DOP in practice, as verified by experimental observations (Piekutowski et al., 1999).

Assuming that the final CRH of the nose approaches 0.5, Mu and Zhang (2011) developed the formulation for the predictions of the upper limit of the nondeformable penetration regime. Table 5 lists the comparison of the transition velocity between the iterative model (denoted as v_s) and the Mu's predictions (denoted as v_p). Clearly, the results available have a high consistency with the scope of the predicted transition velocity from the iterative mass loss model in Case 1 and Case 2. Therefore, it is inferred that the occurrence of the "secondary peak" deceleration can be assumed as a symbol of the upper limit of the nondeformable region. As a response of the change of the nose shape, the "secondary peak" deceleration will greatly affect the performance of projectile, leading to the change of the penetration mechanism. Moreover, the theoretical maximum depth of penetration exists with the corresponding transition velocity, which has been confirmed by Zhao et al. (2010b). As a key parameter for the EPW, increasing the upper limit velocity of the nondeformable region seems to be the crucial approach to the improvement of the EPW's terminal lethality.
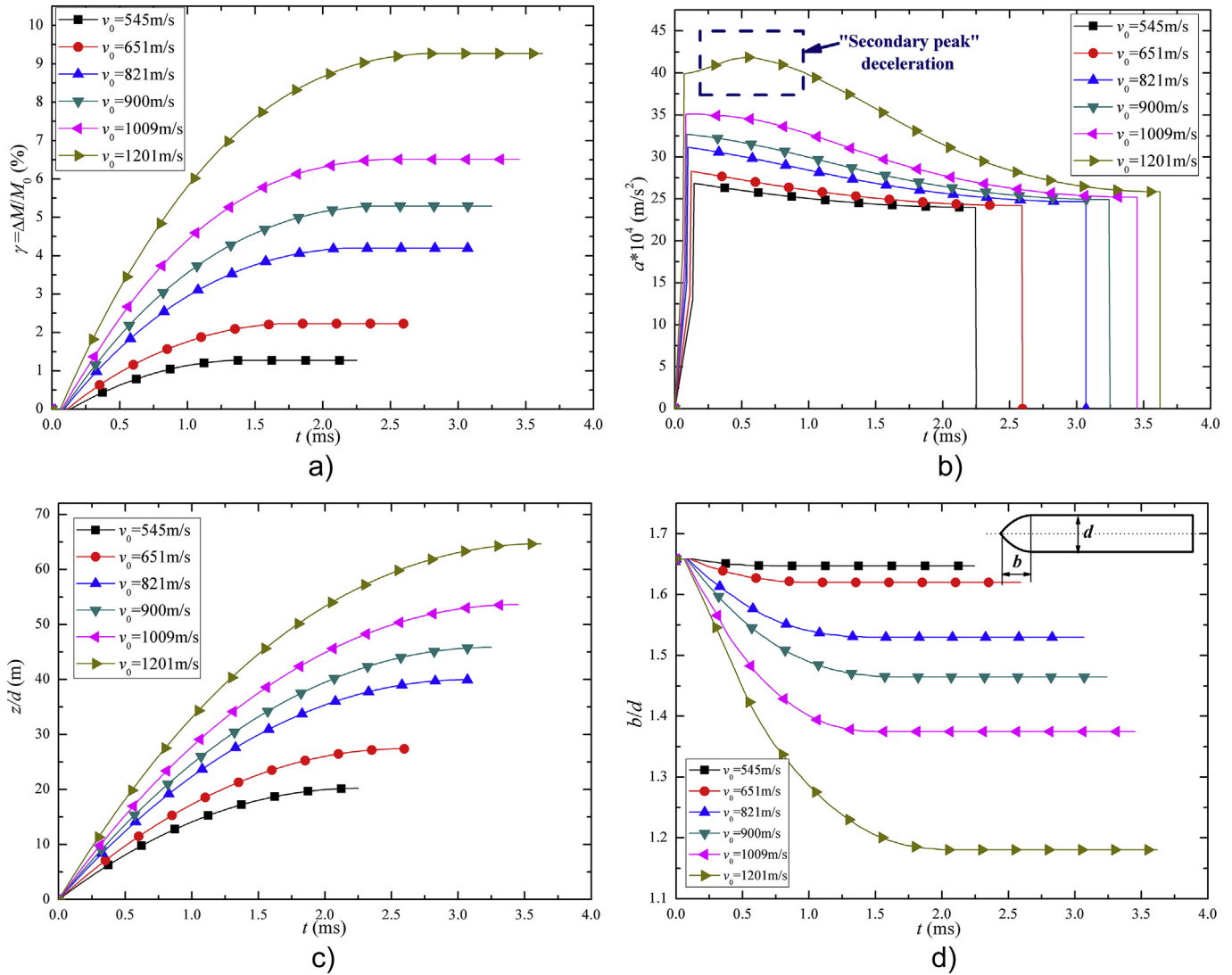
Fig. 14. Calculated time histories of characteristic parameters (a) Percentage of mass loss (b) Deceleration (c) Depth of penetration (d) Nose shape parameter.

4.4. Heat generated by friction and plastic deformation ratio

Based on the failure mechanisms mentioned previously, it is reasonable to consider that the heat generated by friction and plastic deformation is vital to the mass loss of projectile, which is involved in the process of penetration. Further investigation is conducted to reveal the dominant mechanism on mass loss during penetration.

Taking $v_0 = 1009$ m/s in Case 1 for analysis, Fig. 18 (a)- (c) present the temperature gradient generated by friction and plastic deformation along the depth at different surface locations during the penetration process. The observation gauges are labeled as P_A, P_B, and P_C, located at the tip, the middle and the end of the projectile nose, as shown in the upper part of Fig. 18 (a)- (c), respectively. The corresponding instant velocities for $t = 0.15$ ms, 1.54 ms and 3.0 ms are $v = 970$ m/s, 507 m/s and 101 m/s. As discussed above, the heat transfer limits in a very thin surface region during the transient penetration process. As shown in Fig. 18 (a), the depth of the heat affected area by friction is much less than that from the plastic work. However, the magnitude of the temperature generated by friction is greater than that of the plastic work at the initial stage of penetration, which is mainly attributed to the high velocity

sliding with high pressure between projectile and concrete. Clearly, the heat generated by the friction reaches the melt point, while the total temperature rise approaches almost 4500 K (=3000 K + 1500 K) at the exterior surface of nose tip point P_A.

In Fig. 18 (b) and (c), it is noted that both the temperature rises generated by friction and the plastic work conversion decrease with the decline of velocity as expected. It is also interesting to note that the temperature rise caused by friction and the plastic work decreases exponentially along the depth, due to heat conductivity model and the exponential distribution of the effective plastic strain. Almost no difference of the temperature rises between different locations in Fig. 18 (b) and (c) is existed as the instant velocity decreased. The heat generated by the plastic work decreases substantially to a low level due to its pressure characteristics when compared the maximum temperature generated by the plastic work in Fig. 18 (b) and (c).

To further reveal the mechanisms of mass loss at different locations in the projectile, Fig. 18(d) shows the proportion of heat by friction on the exterior surface at the positions P_A, P_B, and P_C at different time intervals. Clearly, the proportion of the heat generated by friction rises to 70% as the penetration progresses from $t = 0.15$ ms to $t = 3.0$ ms, indicating the predominant role of friction
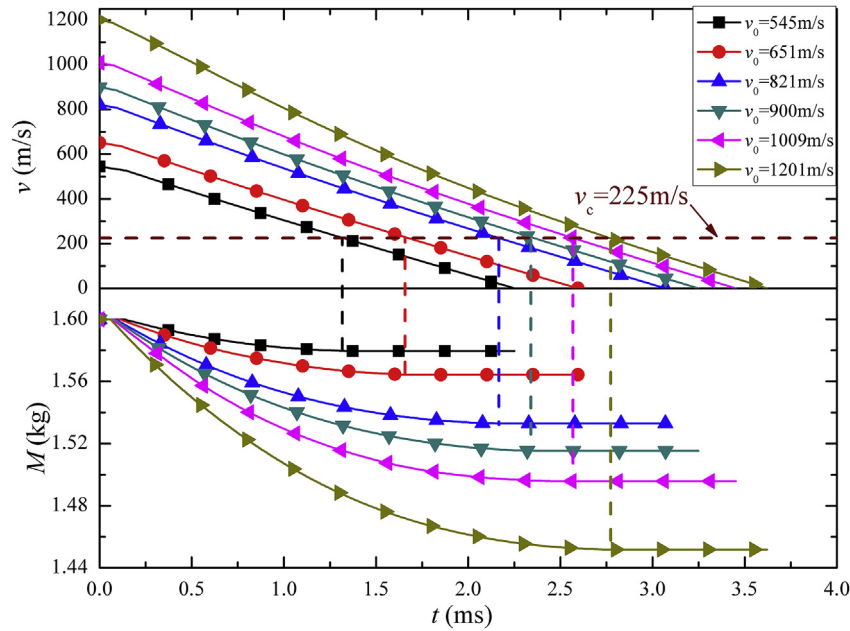
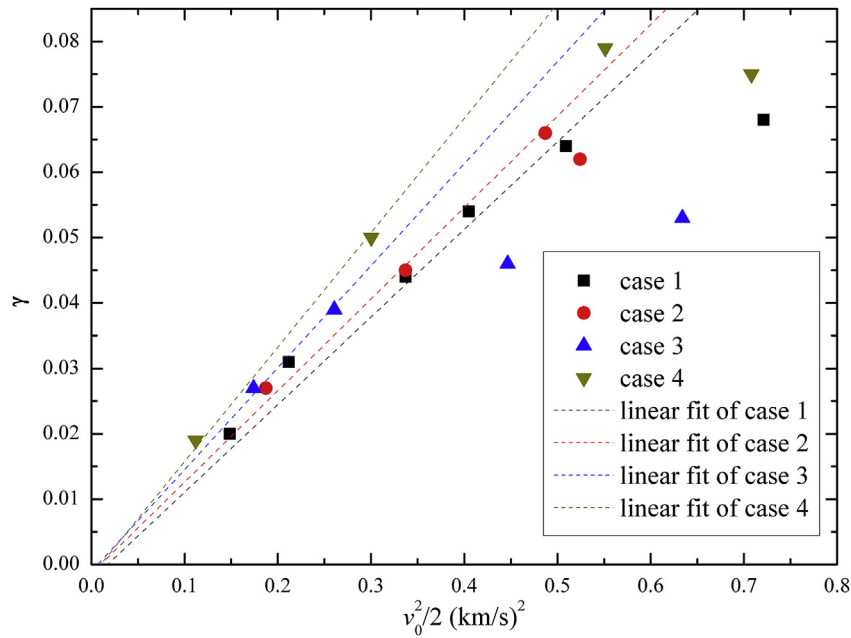**Fig. 15.** Critical velocity of mass loss for Case 1.

Fig. 16. Linear fit between the initial energy and the percentage of mass loss.

Table 4
Critical velocity from the iterative calculations and linear fit data for four penetration events.

	Case 1	Case 2	Case 3	Case 4
Theoretical value v_c from the mass loss iterative model (m/s)	225	204	161	143
Linear fit value v_c based on the experimental data (m/s)	191	151	118	142
Linear fit value C' based on the experimental data (s²/km²)	0.134	0.14	0.156	0.175

in the mass loss, especially at the low velocity period. Due to the temperature limit of the application of the J-C constitutive equations, the heat generated by the plastic work can rise to no more than the melting point of the material. Actually, it can be inferred from the exponential trend in Fig. 18(a) that the heat generated by the plastic work affects the projectile more than that by the friction, showing the dominant effect of the plastic work on the high velocity period. Moreover, it is noted that the heat by the friction plays
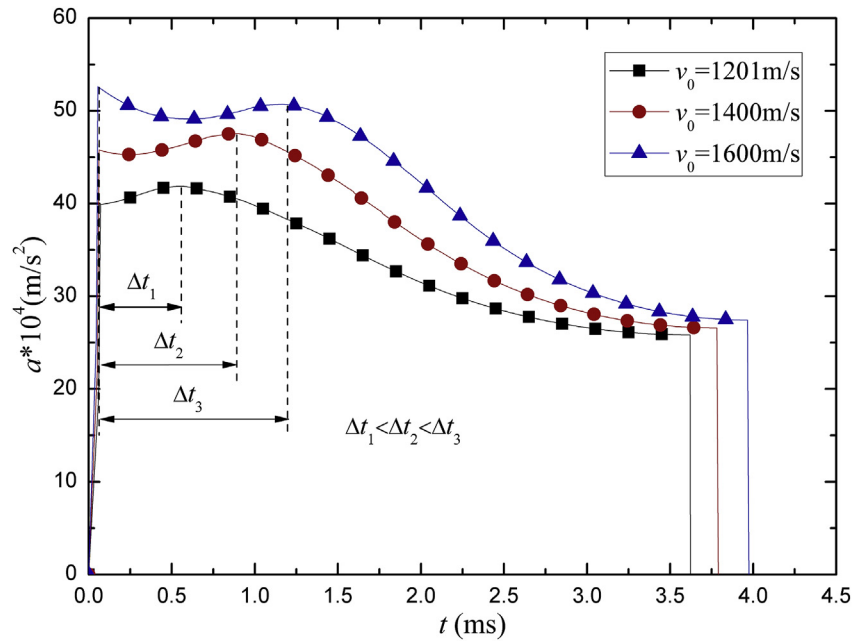
Fig. 17. Deceleration versus time subjected to different impact velocities.

Table 5
The velocity for the occurrence of the "secondary peak" deceleration.

	Case 1	Case 2	Case 3	Case 4
v_s (m/s)	950−1009	987−1024	1126−1250	1190−1250
v_p (m/s)	958	996	−	−

an important role in the mass loss near the shank of the projectile when comparing the proportion of friction heat in P_A, P_B, and P_C at $t = 1.54$ ms and $t = 3.0$ ms. The mass loss at the tip of projectile is determined mainly by the converted plastic work, due to the large plastic strain caused by the high velocity impact. Therefore, the mechanism of the mass loss is the result of the competition between the friction and the plastic work, strongly depending on the contact locations between projectile and concrete.

5. Discussions

Based on the thermoplastic instability failure criteria, an iterative algorithm is proposed to analyze the thermal-mechanical coupled mass loss during the penetration process. The thermodynamic mass abrasion model is proposed for analyzing similar normal penetration process with different impact conditions. Reasonable agreements are obtained between the theoretical predictions and experimental data. Representations of the residual contour of the projectile are demonstrated to present the shape variation of the nose. Parameters that can not be measured experimentally are analyzed to further investigate the penetration process with mass loss. However, due to several underlying assumptions in the model, the dynamic responses related to bending and structural failure are not included in the predictions. The fracture of the material cannot be predicted in this model, resulting in the sharp nose of the final projectile, which seems unpractical. The model is also unable to calculate the asymmetric mass loss and the deviation of the terminal trajectory, which is complicated when taking into account the random distribution characteristics of the aggregate in the concrete. These will be the valuable work for future research.

5.1. The valid velocity range for the EPW

The key factors determining the material failure are closely related to the material properties at high temperature, high pressure and high strain-rate. During the penetration, the stress, strain and strain-rate decrease from the maximum at the exterior surface to approximately zero in the matrix, presenting a gradient distribution in a thin area on the surface of a projectile. Moreover, coupled with the temperature-based ductile failure criterion, different receding displacements are derived from the iterative calculations, which result in blunting the nose of the projectile. Compared with the rigid projectile, the change of the nose shape has a great influence on the high velocity penetration. The velocity regime, including the lower and the upper limit for the non-deformable penetration, is determined according to the feature of the penetration process. The onset of the mass loss is determined at the lower limit velocity of the nondeformable penetration regime. This threshold value is closely related to the interactions between the projectile nose and the target medium. On the other hand, structure failure, trajectory deviation and dramatic drop of DOP appear when exceeding the upper limit velocity of the non-deformable penetration regime with the occurrence of the "secondary peak" deceleration. Intensive vibration and increase of the deceleration will likely appear simultaneously. The valid velocity range is applicable for the EPW, within which the DOP and the percentage of mass loss increase stably as the enhancement of impact velocity. Increasing the upper limit velocity is a useful approach for the enchantment of the depth of penetration.

5.2. The dominant mechanism of mass loss

The dominant factors between the dynamic friction and the converted plastic work are investigated to further reveal the mechanisms of mass loss during the high velocity penetration. It is demonstrated that the heat generated by the plastic work is the dominant factor to the mass loss when the instant velocity is comparatively high. Located in a thin layer area of the exterior surface, the heat generated by friction plays a dominant role in the
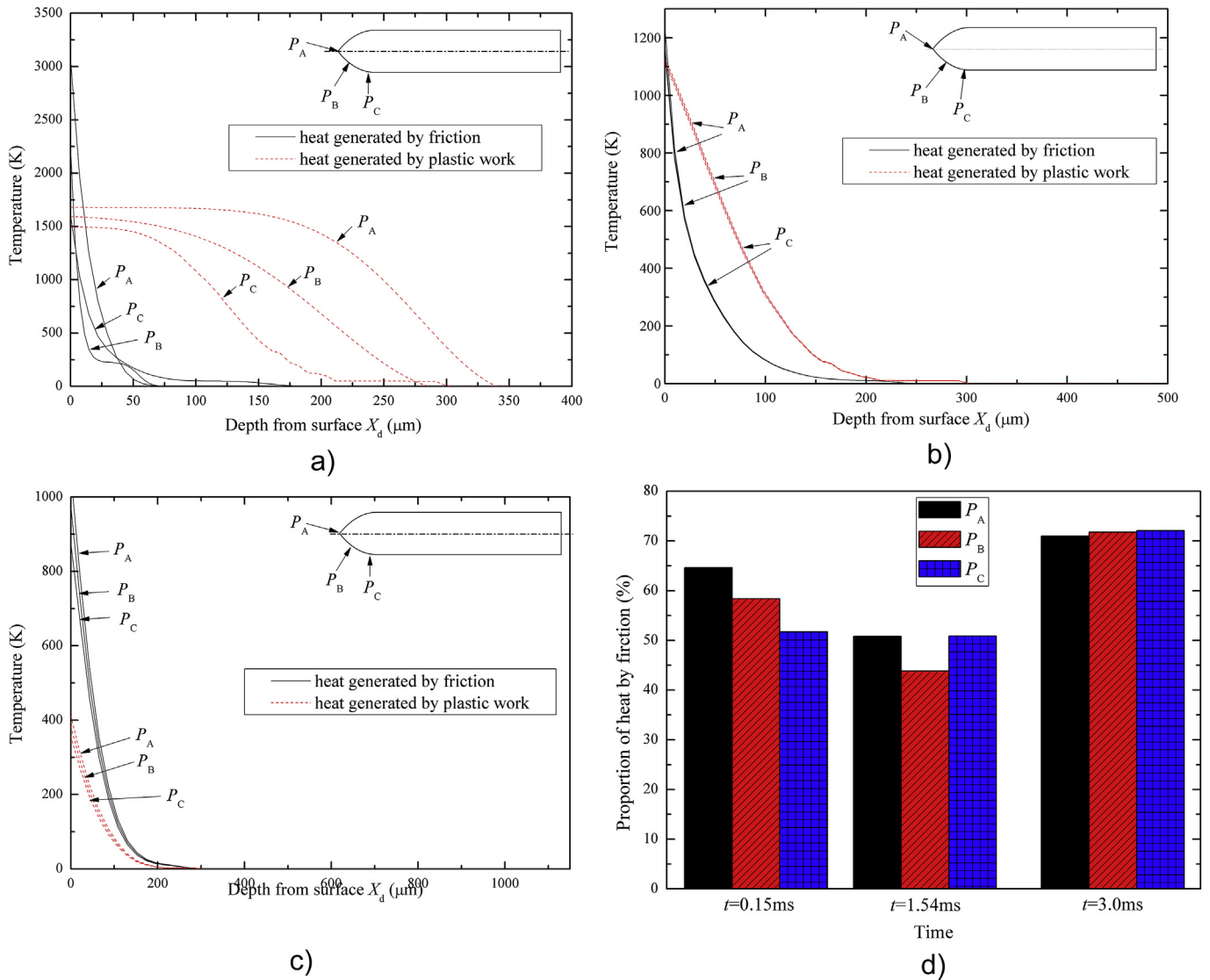
Fig. 18. Temperature rising generated by friction and plastic work (a) $t = 0.15$ ms (b) $t = 1.54$ ms (c) $t = 3.0$ ms (d) proportion of the heat by friction.

low velocity penetration, which cannot be ignored. The temperature rise reaches the melt point in the beginning of the penetration process, resulting in serious mass loss of the projectile. Comparing the proportion of heat sources in different locations, it can be inferred that the heat due to the friction plays a dominant role in the mass loss near the shank of projectile, which is very important for designing the reduction of mass loss effectively.

6. Conclusions

In this study, based on the mechanisms of thermoplastic failure, a thermal dynamic mass loss model is proposed and developed to investigate the high velocity penetration process with mass loss. Utilizing spatial and temporal discretization, the transient penetration process is discrete to calculate the movement and the variations of the nose. Also, coupled with the temperature-based failure criterion, the localized temperature rises generated by the dynamic friction and the plastic work are combined together to find the receding displacements, resulting in the nose variations of the projectile. Good agreements have been obtained between the predictions and the experimental data, including the shape of nose,

the mass loss and the DOP. Basic phenomenon such as the nose abrasion and the drop of the DOP are analyzed and compared with the rigid penetration. Further investigations have been conducted on the modified valid velocity range, mainly focused on the lower and upper velocity limit of the nondeformable penetration regime. In addition, the characteristics of its occurrence are analyzed theoretically, including the critical velocity of mass loss and the appearance of the "Secondary peak" deceleration. The dominant factors that result in the heat are compared with the temperature distributions along the depth at different locations of the projectile during penetration. The method presented is useful for the understanding of the high velocity penetration process with mass loss.

University of Science and Technology (2013_ZJ_0101) and the China Scholarship Council (CSC) for their great support on the research work presented in this paper.

References

Alekseevskii, V.P., 1966. Penetration of a rod into a target at high velocity. Combust. Explos. Shock Waves 2 (2), 63—66.

Archard, J.F., 1959. The temperature of rubbing surfaces. Wear 2 (6), 438—455.

Bai, Y.L., 1982. Thermo-plastic instability in simple shear. J. Mech. Phys. Solids 30 (4), 195—207.

Bai, Y.L., Dodd, B., 1992. Adiabatic Shear Localization: occurrence, theories, and applications. Pergamon Press.

Beissel, S.R., Johnson, G.R., 2000. An abrasion algorithm for projectile mass loss during penetration. Int. J. Impact Eng. 24 (2), 103—116.

Beissel, S.R., Johnson, G.R., 2002. A three-dimensional abrasion algorithm for projectile mass loss during penetration. Int. J. Impact Eng. 27 (7), 771—789.

Blok, H., 1963. The flash temperature concept. Wear 6 (6), 483—494.

Bowden, F.P., Persson, P.A., 1961. Deformation, heating and melting of solids in high-speed friction. Math. Phys. Sci. 260 (1303), 433—458.

Campbell, G.S., Calissendorff, C., Williams, J.H., 1991. Probe for measuring soil specific heat using a heat-pulse method. Soil Sci. Soc. Am. J. 55 (1), 291—293.

Chen, X.W., Li, Q.M., 2004. Transition from nondeformable projectile penetration to semi hydrodynamic penetration. J. Eng. Mech. 130 (1), 123—127.

Chen, X.W., Li, J.C., 2014. Analysis on the resistive force in penetration of a rigid projectile. Def. Technol. 10 (3), 285—293.

Chen, X.W., He, L.L., Yang, S.Q., 2010. Modeling on mass abrasion of kinetic energy penetrator. Eur. J. Mechanics-A/Solids 29 (1), 7—17.

Clifton, R.J., Duffy, J., Hartley, K.A., Shawki, T.G., 1984. On critical conditions for shear band formation at high strain rates. Scr. Metall. 18 (5), 443—448.

Davis RN, Jones SE, Hughes ML. High-speed penetration of concrete using a new analytical model of velocity-dependent friction. ASME 2003 Pressure Vessels and Piping Conference, Cleveland, 2003, 454: 111—116.

Fleck, N.A., Muller, G.M., Ashby, M.F., Hutchinson, J.W., 1994. Strain gradient plasticity: theory and experiment. Acta Metallurgica Materialia 42 (2), 475—487.

Forrestal, M.J., Luk, V.K., 1992. Penetration into soil targets. Int. J. Impact Eng. 12 (3), 427—444.

Forrestal, M.J., Tzou, D.Y., 1997. A spherical cavity-expansion penetration model for concrete targets. Int. J. Solids Struct. 34 (31), 4127—4146.

Forrestal, M.J., Okajima, K., Luk, V.K., 1988. Penetration of 6061-T651 aluminum targets with rigid long rods. J. Appl. Mech. 55 (4), 755—760.

Forrestal, M.J., Altman, B.S., Cargile, J.D., Hanchak, S.J., 1994. An empirical equation for penetration depth of ogive-nose projectiles into concrete targets. Int. J. Impact Eng. 15 (4), 395—405.

Forrestal, M.J., Frew, D.J., Hanchak, S.J., Brar, N.S., 1996. Penetration of grout and concrete targets with ogive-nose steel projectiles. Int. J. Impact Eng. 18 (5), 465—476.

Forrestal, M.J., Frew, D.J., Hickerson, J.P., Rohwer, T.A., 2003. Penetration of concrete targets with deceleration-time measurements. Int. J. Impact Eng. 28 (5), 479—497.

Frew, D.J., Hanchak, S.J., Green, M.L., Forrestal, M.J., 1998. Penetration of concrete targets with ogive-nose steel rods. Int. J. Impact Eng. 21 (6), 489—497.

Frew, D.J., Forrestal, M.J., Hanchak, S.J., 2000. Penetration experiments with limestone targets and ogive-nose steel projectiles. J. Appl. Mech. 67 (4), 841—845.

Frew, D.J., Forrestal, M.J., Cargile, J.D., 2006. The effect of concrete target diameter on projectile deceleration and penetration depth. Int. J. Impact Eng. 32 (10), 1584—1594.

Guo, L., He, Y., Zhang, X.F., Pang, C.X., Qiao, L., Guan, Z.W., 2014. Study mass loss at microscopic scale for a projectile penetration into concrete. Int. J. Impact Eng. 72, 17—25.

He, L.L., Chen, X.W., 2011a. Analyses of the penetration process considering mass loss. Eur. J. Mechanics-A/Solids 30 (2), 145—157.

He, L.L., Chen, X.W., 2011b. Simulation of variation of projectile nose during high-speed penetration into concrete. Chinses J. Theor. Appl. Mech. 43 (4), 707—715.

He, X., Xu, X.Y., Sun, G.J., Shen, J., Yang, J.C., Jin, D.L., 2010. Experimental investigation on projectiles' high-velocity penetration into concrete targets. Explos. Shock Waves 30 (1), 1—6.

He, L.L., Chen, X.W., He, X., 2010. Parametric study on mass loss of penetrators. Acta Mech. Sin. 26 (4), 585—597.

He, L.L., Chen, X.W., Xia, Y.M., 2014. Representation of nose blunting of projectile into concrete target and two reduction suggestions. Int. J. Impact Eng. 74, 132—144.

Heilmann, P., Rigney, D.A., 1981. An energy-based model of friction and its application to coated systems. Wear 72 (2), 195—217.

Johnson GR, Cook WH. A constitutive model and data for metals subjected to large strains, high strain rates and high temperatures. Proceedings of the 7th International Symposium on Ballistics. Netherlands, 1983, 21: 541—547.

Jones, S.E., Rule, W.K., 2000. On the optimal nose geometry for a rigid penetrator, including the effects of pressure-dependent friction. Int. J. Impact Eng. 24 (4), 403—415.

Jones SE, Foster JC, Toness OA, DeAngelis RJ, Rule WK. An estimate for mass loss from high velocity steel penetrators. Proceedings of the ASME PVP-435 Conference on Thermal-Hydraulic Problems, Sloshing Phenomena, and Extreme Loads on Structures, New York, 2002, 422:227—237.

Jones SE, Davis RN, Hughes ML, Toness OA. Penetration with high-speed friction, ASME 2002 pressure vessels and piping conference. Vancouver, 2002: 255—262.

Jones, S.E., Hughes, M.L., Toness, O.A., Davis, R.N., 2003. A one-dimensional analysis of rigid-body penetration with high-speed friction. Proceedings of the Institution of Mechanical Engineers, Part C: J. Mech. Eng. Sci. 217 (4), 411—422.

Kennedy, R.P., 1976. A review of procedures for the analysis and design of concrete structures to resist missile impact effects. Nucl. Eng. Des. 37 (2), 183—203.

Klepaczko, J.R., 2001. Surface Layer Thermodynamics of Steel Penetrators at High and Very High Sliding Velocities. Florida University Shalimar Graduate Engineering and Research Center.

Klepaczko, J.R., Hughes, M.L., 2005. Scaling of wear in kinetic penetrators. Int. J. Impact Eng. 31 (4), 435—459.

Krafft, J.M., 1955. Surface friction in ballistic penetration. J. Appl. Phys. 26 (10), 1248—1253.

Li, Q.M., Chen, X.W., 2003. Dimensionless formulae for penetration depth of concrete target impacted by a non-deformable projectile. Int. J. Impact Eng. 28 (1), 93—116.

Li, S., Liu, W.K., Qian, D., Guduru, P.R., Rosakis, A.J., 2001. Dynamic shear band propagation and micro-structure of adiabatic shear band. Comput. Methods Appl. Mech. Eng. 191 (1), 73—92.

Lu, X., 2002. Nonequilibrium Thermodynamic Models for the Dynamic Behavior of Polycrystalline Solids. PhD Thesis. Georgia Institute of Technology.

Luk, V.K., Forrestal, M.J., 1987. Penetration into semi-infinite reinforced-concrete targets with spherical and ogival nose projectiles. Int. J. Impact Eng. 6 (4), 291—301.

Lundgren RG. High-velocity penetrators. Presented at the American Institute of Aeronautics and Astronautics Missile Sciences Conference, Monterey, CA, 7-9 Nov. 1994. 1994, 1: 7—9.

Magness, L.S., 1994. High strain rate deformation behaviors of kinetic energy penetrator materials during ballistic impact. Mech. Mater. 17 (2), 147—154.

Medyanik, S.N., Liu, W.K., Li, S., 2007. On criteria for dynamic adiabatic shear band propagation. J. Mech. Phys. Solids 55 (7), 1439—1461.

Molinari, A., Clifton, R.J., 1987. Analytical characterization of shear localization in thermoviscoplastic materials. J. Appl. Mech. 54 (4), 806—812.

Montgomery, R.S., 1976. Friction and wear at high sliding speeds. Wear 36 (3), 275—298.

Mu, Z.C., Zhang, W., 2011. An investigation on mass loss of ogival projectiles penetrating concrete targets. Int. J. Impact Eng. 38 (8—9), 770—778.

Oxley, P.L.B., Hastings, W.F., 1977. Predicting the strain rate in the zone of intense shear in which the chip is formed in machining from the dynamic flow stress properties of the work material and the cutting conditions. Proceedings of the Royal Society of London. A 356 (1686), 395—410.

Piekutowski, A.J., Forrestal, M.J., Poormon, K.L., et al., 1999. Penetration of 6061-T6511 aluminum targets by ogive-nose steel projectiles with striking velocities between 0.5 and 3.0 km/s. Int. J. Impact Eng. 23 (1), 723—734.

Rigney, D.A., Hirth, J.P., 1979. Plastic deformation and sliding friction of metals. Wear 53 (2), 345—370.

Rigney, D.A., Chen, L.H., Naylor, M.G.S., Rosenfield, A.R., 1984. Wear processes in sliding systems. Wear 100 (1), 195—219.

Rosakis, A.J., Ravichandran, G., 2000. Dynamic failure mechanics. Int. J. Solids Struct. 37 (1), 331—348.

Rosenberg, Z., Dekel, E., 2009. The penetration of rigid long rods—revisited. Int. J. Impact Eng. 36 (4), 551—564.

Schoenfeld, S.E., Wright, T.W., 2003. A failure criterion based on material instability. Int. J. Solids Struct. 40 (12), 3021—3037.

Silling, S.A., Forreatal, M.J., 2007. Mass loss from abrasion on ogival-nose steel projectile that penetrate concrete targets. Int. J. Impact Eng. 34 (11), 1814—1820.

Tate, A., 1967. A theory for the deceleration of long rods after impact. J. Mech. Phys. Solids 15 (6), 387—399.

Tounsi, N., Vincenti, J., Otho, A., Elbestawi, M.A., 2002. From the basic mechanics of orthogonal metal cutting toward the identification of the constitutive equation. Int. J. Mach. Tools Manuf. 42 (12), 1373—1383.

Wang, X.B., 2006. Effects of constitutive parameters on adiabatic shear localization for ductile metal based on JOHNSON-COOK and gradient plasticity models. Trans. Nonferrous Metals Soc. China 16 (6), 1362—1369.

Wen, H.M., Yang, Y., He, T., 2010. Effects of abrasion on the penetration of ogival-nosed projectiles into concrete targets. Lat. Am. J. Solids Struct. 7 (4), 413—422.

Wright, T.W., 2002. The Physics and Mathematics of Adiabatic Shear Bands. Cambridge University Press.

Wu, H.J., Huang, F.L., Wang, Y.N., Duan, Z.P., Shan, Y., 2012. Mass loss and nose shape change on ogive-nose steel projectiles during concrete penetration. Int. J. Nonlinear Sci. Numer. Simul. 13 (3), 273—280.

Yang, J.C., Zuo, X.J., He, X., Jin, D.L., 2012. Experimental study of projectile mass loss in high velocity penetration of concrete target. J. Exp. Mech. 27 (1), 122—127.

Yang, Y., He, T., Wen, H.M., 2012. An abrasion algorithm for ogive-nose steel projectile penetrating concrete target. Chin. J. High Press. Phys. 26 (1), 83—88.

Zener, C., Hollomon, J.H., 1944. Effect of strain rate upon plastic flow of steel. J. Appl. Phys. 15 (1), 22—32.

Zhao, J., Chen, X.W., Jin, F.N., Xu, Y., 2010. Depth of penetration of high-speed penetrator with including the effect of mass abrasion. Int. J. Impact Eng. 37

(9), 971–979.

Zhao, J., Chen, X.W., Jin, F.N., et al., 2010. Depth of penetration of high-speed penetrator with including the effect of mass abrasion. Int. J. Impact Eng. 37 (9), 971–979.

Zhao, J., Chen, X.W., Jin, F.N., Xu, Y., 2012. Analysis on the bending of a projectile induced by asymmetrical mass abrasion. Int. J. Impact Eng. 39 (1), 16–27.

Zhou, M., Ravichandran, G., Rosakis, A.J., 1996. Dynamically propagating shear bands in impact-loaded prenotched plates—II. Numerical simulations. J. Mech. Phys. Solids 44 (6), 1007–1032.